JMEPEG (2015) 24:221–228
DOI: 10.1007/s11665-014-1273-4

1059-9495/$19.00

Prediction of Ductile Fracture Behaviors for 42CrMo Steel at Elevated Temperatures

Y.C. Lin, Yan-Xing Liu, Ge Liu, Ming-Song Chen, and Yuan-Chun Huang

(Submitted July 12, 2014; in revised form September 6, 2014; published online October 22, 2014)

The ductile fracture behaviors of 42CrMo steel are studied by hot tensile tests with the deformation temperature range of 1123-1373 K and strain rate range of 0.0001-0.1 s^{-1}. Effects of deformation temperature and strain rate on the flow stress and fracture strain of the studied steel are discussed in detail. Based on the experimental results, a ductile damage model is established to describe the combined effects of deformation temperature and strain rate on the ductile fracture behaviors of 42CrMo steel. It is found that the flow stress first increases to a peak value and then decreases, showing an obvious dynamic softening. This is mainly attributed to the dynamic recrystallization and material intrinsic damage during the hot tensile deformation. The established damage model is verified by hot forging experiments and finite element simulations. Comparisons between the predicted and experimental results indicate that the established ductile damage model is capable of predicting the fracture behaviors of 42CrMo steel during hot forging.

Keywords 42CrMo steel, damage model, ductile fracture, finite element simulations

1. Introduction

The ductile damage, such as an internal or surface fracture in the workpiece, may be often observed during the metal forming if the processing parameters are not reasonably controlled. So, the ductile damage is generally considered as a vital index of formability (Ref 1-3). Finding a way to evaluate the ductile fracture behaviors and identify the relationships between the damage evolution and processing parameters are very important.

In order to predict the material failure behaviors during the metal forming, a number of ductile fracture criteria have been developed. These criteria can be divided into two categories: the physically based and phenomenological fracture criteria. Although the physically based fracture criteria may offer a comprehensive description of the fracture process, several material parameters have to be calibrated and the complicated testing procedures are required (Ref 4). Due to their simple formulation and ease of calibration, the phenomenological fracture criteria have been widely used in industry. Most of them relate to the critical plastic work per unit of volume, such as the Freudenthal criterion, Cockcroft-Latham criterion, and Normalized Cockcroft-Latham criterion (Ref 5, 6). In these ductile fracture criteria, the fracture is assumed to initiate when the critical plastic work is reached. However, the application of these conventional ductile fracture criteria in the hot working process is limited. Because they were originally developed for the cold forming process, the effects of hot working parameters on the deformation behaviors of materials were not fully taken into account. In fact, the effects of deformation temperature and strain rate on the ductile fracture are significant, which should be considered when the ductile fracture criterion is established. Considering the combined effects of deformation temperature and strain rate on the ductile fracture behaviors, the suitable ductile fracture criteria have been established for 3Cr20Ni10W2 alloy (Ref 7), Ti40 alloy (Ref 8, 9), 30Cr2Ni4-MoV ultra-super-critical rotor steel (Ref 10), and magnesium alloys (Ref 11). Yoon and Lee (Ref 12) found that the fracture mechanism changes from brittle to ductile with increase of the forming temperature for AZ31 magnesium alloy sheet. Paul and Kumar (Ref 13, 14) employed a micromechanics-based approach by means of representative volume element to predict the flow behavior, plastic strain localization, and plastic instability of dual phase steels. Shore et al. (Ref 15) optimized the hot forming parameters for Incoloy 901 alloy to avoid the risk of premature fracture.

42CrMo steel (American grade: AISI 4140) is a representative medium carbon and low alloy steel, which is widely used for many general purpose parts including the automotive crankshaft, rams, etc. (Ref 16, 17). The preferential use of 42CrMo high-strength steel is attributed to its good balance of strength, toughness, and water resistance (Ref 18, 19). In order to study the workability and establish the optimum hot forming parameters for 42CrMo steel, the compressive/tension deformation behaviors of 42CrMo steel were investigated over wide ranges of forming temperature and strain rate (Ref 20-35). The static (Ref 20, 21), dynamic (Ref 22-24), and metadynamic (Ref 25-27) recrystallization behaviors of 42CrMo steel have been studied. Meanwhile, the constitutive relation is generally established to describe the relationship between the flow stress and deformation parameters (Ref 1, 28). Based on the experimental results, some physically based and

Y.C. Lin, Yan-Xing Liu, Ge Liu, Ming-Song Chen, and **Yuan-Chun Huang,** School of Mechanical and Electrical Engineering, Central South University, Changsha 410083, China; and State Key Laboratory of High Performance Complex Manufacturing, Changsha 410083, China. Contact e-mails: yclin@csu.edu.cn and linyongcheng@163.com.

Fig. 1 Hot tensile testing apparatus and fractured specimen

phenomenological constitutive models are proposed to accurately describe the plastic deformation characteristics of 42CrMo steel, and these constitutive models are critical for the correct numerical simulation and the reasonable optimization of hot forming process (Ref 29-31). Chen et al. (Ref 32) studied the effects of tempering temperature on the impact toughness of 42CrMo steel. Li et al. (Ref 33) proposed a novel open-die warm extrusion process of spline shaft with 42CrMo steel to solve the process problems, such as high forming loads, poor material plasticity, and tooth filled quality. Wang et al. (Ref 34) investigated the austenite grain growth behaviors of 42CrMo steel through heat insulation tests, and established a reliable mathematical model for predicting the average austenite grain size at constant temperature. Qian et al. (Ref 35) investigated the radial-axial ring rolling process for 42CrMo steel large-scale rings, and discussed the effects of roll sizes on the radial-axial ring rolling process. Although large amount of efforts have been devoted to understanding the hot deformation behaviors of 42CrMo steel, little attention has been given to predict the ductile fracture behavior of this material during the hot working (Ref 36). In order to produce sound and reliable forgings, an accurate prediction of ductile fracture behavior is necessary for optimizing the processing parameters.

In the present study, the ductile fracture behaviors of 42CrMo steel are investigated by uniaxial hot tensile tests. A ductile damage model is established to predict the fracture behaviors of 42CrMo steel during the hot working. The capability of the established ductile damage model is validated by hot forging experiments and finite element simulations.

Table 1 Chemical compositions of 42CrMo steel (wt.%)

Cr	Mn	C	Si	Mo	P	Cu	S	Fe
0.960	0.630	0.450	0.280	0.190	0.016	0.014	0.012	Bal.

2. Experiments and Finite Element Simulations

2.1 Hot Tensile Tests

Commercial 42CrMo steel was investigated in this study. The chemical compositions (wt.%) of the studied material are listed in Table 1. Cylindrical specimens were machined from the ingot bar according to the international standard: ISO 6892-2 (Ref 37). Also, according to ISO 6892-2, the suitable testing procedures were designed. Hot tensile tests were carried out on an INSTRON machine. Four different deformation temperatures (1123, 1223, 1323, and 1373 K) and four different strain rates (0.1, 0.01, 0.001, and 0.0001 s^{-1}) were selected. The gage length and diameter of specimen are 25 and 10 mm, respectively. Firstly, the specimens were heated to the deformation temperature at a heating rate of 10 K/mm and held for 20 min before loading. Then, the specimens were stretched under the designed deformation temperatures and strain rates. Figure 1 shows the hot tensile testing apparatus and fractured specimen.

2.2 Hot Forging Experiments

Using the experimental results from hot tensile tests, a ductile damage model was first established based on the Normalized Cockcroft-Latham criterion. Then, hot forging experiments and the corresponding finite element simulations were conducted to verify the established ductile damage model. According to the practice industry criterion, the deformation temperatures of hot forging experiments were selected as 1473 and 1223 K. Rectangular workpiece with the dimensions of 50 mm × 50 mm × 120 mm were compressed between two flat dies on a four-column type hydraulic press with a nominal force of 3150 KN, as shown in Fig. 2. Prior to the hot forging experiments, the workpiece were heated to the deformation temperature and held in the electric resistance furnace for 30 min. In order to avoid the oxidation of workpieces' surface, the deformed workpieces were immediately put into sands, and cooled to the room temperature after forging experiments.

2.3 Finite Element Simulations

The finite element simulations for hot forging experiments were carried out using the commercial software DEFORM-3D. Before simulation, the established ductile damage model was firstly implemented into DEFORM-3D by the user subroutine. Figure 3 shows the finite element model used in the simulations. The workpiece was meshed with tetrahedron element and fine meshes were generated in the deformation zone. Both the upper and lower dies were regarded as rigid objects. The process conditions in the finite element simulation are: (i) The friction coefficient between the workpiece and dies is 0.7 in terms of shear friction; (ii) the temperature of environment is assumed as the room temperature (293 K); (iii) the heat transfer coefficient between the workpiece and dies is 5 N/s/mm/K, the convection coefficient to environment is 0.02 N/s/mm/K.

2.4 Experimental Result and Discussion

Generally, the true stress-true strain curve is always used to analyze the plastic deformation properties of materials (Ref 1, 38, 39). Figure 4 shows the typical hot tensile true stress-strain curves of 42CrMo steel under different deformation conditions. From Fig. 4, it can be easily found that the effects of deformation temperature and strain rate on the flow behaviors of 42CrMo steel are significant. The flow stress decreases with

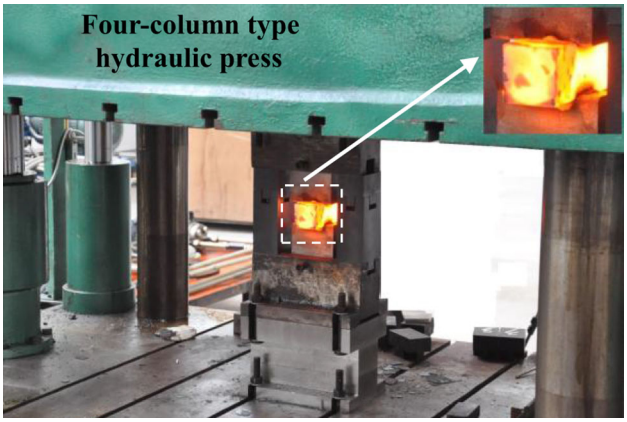

Fig. 2 Hot forging experiments: (a) four-column type hydraulic press; (b) deformed workpiece

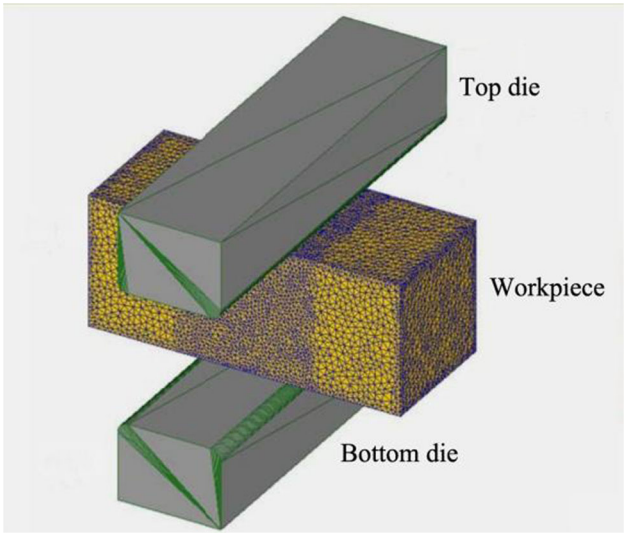

Fig. 3 Finite element model for the forging experiment

the increase of deformation temperature or the decrease of strain rate. This is because the high temperature promotes the nucleation and growth of dynamically recrystallized grains and dislocation annihilation (Ref 40, 41), while the low strain rate results in long time for energy accumulation. Some new grain structures are formed via the formation and migration of high-angle grain boundaries driven by the stored energy of deformation (Ref 23, 24). Meanwhile, the driving force for this migration reduces the grain-boundary area itself during the deformation process. Thus, the flow stress decreases. As shown in Fig. 4(a), under relatively high strain rates (0.01 and 0.1 s^{-1}), the flow stress firstly increases to the peak value and then sharply decreases till the final fracture, showing the obvious work hardening and dynamic softening stages. However, under relatively low strain rates (0.0001 and 0.001 s^{-1}), the flow stress increases to a peak value, and then follows a quasi-stable deformation stage. The fluctuations of flow stresses during the quasi-stable deformation stage result from the combined effects of the work hardening, dynamic recovery, and dynamic recrystallization, as well as the synthetical effects of localized necking and microvoid coalescence (Ref 2, 3, 42, 43).

Fracture strain can be used to evaluate the ductility of metals or alloys (Ref 2, 3). Figure 5 shows the relationships between the fracture strain (ε_f) and deformation temperature under different strain rates. Obviously, the fracture strains are very sensitive to the deformation temperature and strain rate. Under relatively high strain rates (0.01 and 0.1 s^{-1}), the fracture strain firstly increases, and then decreases with increasing the deformation temperature. The reason for this phenomenon is that the dynamic recrystallization easily takes place with the increase of deformation temperature, which results in the fine grains (Ref 44). So, the fracture strain increases correspondingly. i.e., the ductility of the material is improved by the fine dynamic recrystallized structure. Also, some other researchers (Ref 45, 46) found that the dynamic recrystallization is the reason for the improvement of ductility of alloys when the deformation temperature is relatively high. However, as the deformation temperature is continually increased, the dynamic recrystallized grain coarsens which weakens the plastic deformation capability of the material, and the relatively small fracture strains appear. While under relatively low strain rates (0.0001 and 0.001 s^{-1}), the fracture strain decreases monotonously with the increase of deformation temperature. This is because the dynamic recrystallization takes place under the tested conditions, and the low strain rate easily makes the fine recrystallized grains grow up rapidly, which deteriorates the ductility of the material.

3. Establishment of Ductile Damage Model for 42CrMo Steel

The basic form of phenomenological ductile fracture criterion can be expressed as,

$$\int_0^{\varepsilon_f} f(\sigma_{ij})d\varepsilon = C, \qquad \text{(Eq 1)}$$

where $f(\sigma_{ij})$ is a function of flow stress, ε_f is the fracture strain, and C is a material constant (a threshold value).

Within the framework of isotropic continuum damage mechanics, the damage evolution of material can be described by a scalar variable ψ, and the evolution equation of damage can be expressed as (Ref 47),

$$\dot{\psi} = -\frac{Y}{S}\dot{\varepsilon}, \qquad \text{(Eq 2)}$$

where $\dot{\psi}$ is the damage evolution rate, Y is the damage strain energy release rate, S is the damage strength parameter that can be experimentally determined for a given material, and $\dot{\varepsilon}$ is the strain rate. Assuming $S = 1$ and $Y = f(\sigma_{ij})$, then Eq 1 can be obtained by integrating both sides of Eq 2 with respect to time until the final fracture. Moreover, Y is the key state variable in determining damage evolution rate $\dot{\psi}$, while the damage strength parameter S is mainly used to normalize the strain energy release rate Y. Therefore, the physical meaning of S can be regarded as the damage resistance. If Y is a function of flow stress that is sensitive to the deformation temperature and strain rate (Ref 48), then S should be also a function of these two variables,

$$S = S(T, \dot{\varepsilon}) \qquad \text{(Eq 3)}$$

Substituting Eq 3 into 2, the damage variable ψ for ductile fracture can be expressed as,

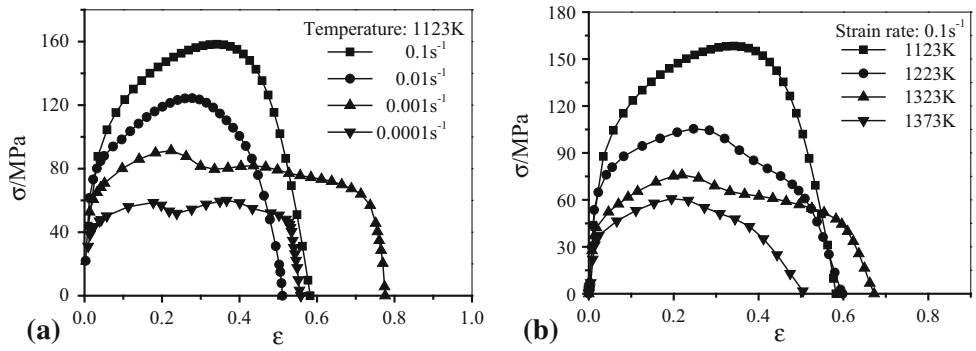

Fig. 4 Typical hot tensile true stress-strain curves under: (a) $T = 1123$ K; (b) $\dot{\varepsilon} = 0.1$ s^{-1}

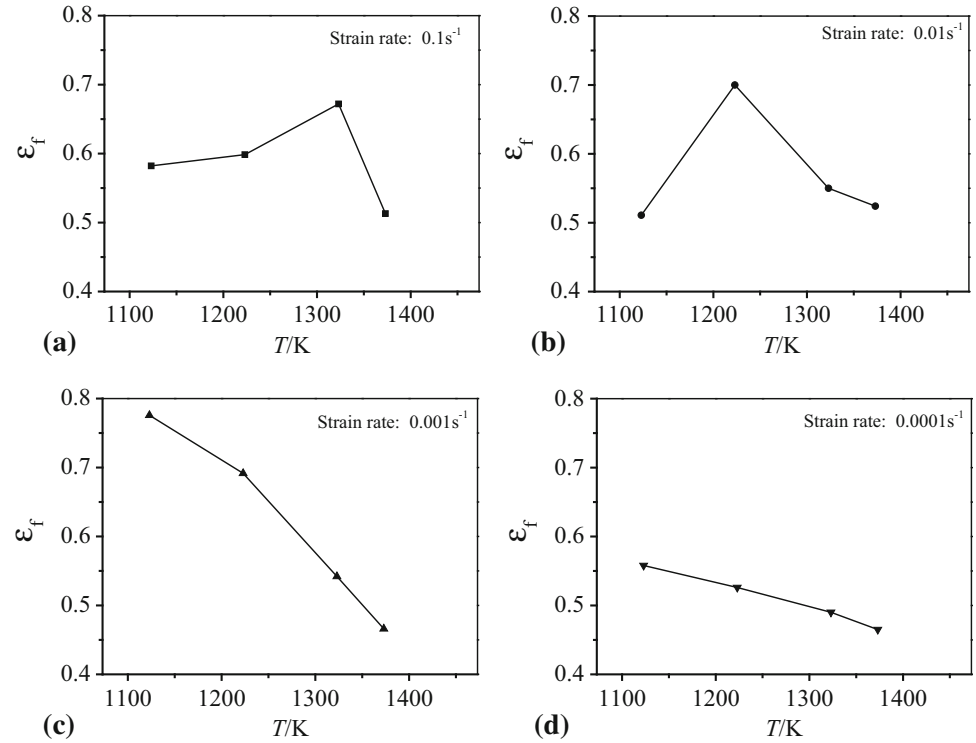

Fig. 5 Relationships between the fracture strain (ε_f) and deformation temperature (T) under the strain rates of: (a) 0.1 s^{-1}; (b) 0.01 s^{-1}; (c) 0.001 s^{-1}; (d) 0.0001 s^{-1}

$$\psi = \int_0^t \dot{\psi} \mathrm{d}t = \int_0^t \frac{Y}{S(T,\dot{\varepsilon})} \dot{\varepsilon} \mathrm{d}t = \int_0^{\varepsilon} \frac{Y}{S(T,\dot{\varepsilon})} \mathrm{d}\varepsilon, \qquad \text{(Eq 4)}$$

where t is the deformation time. Then, the ductile fracture criterion can be given as,

$$\psi_f = \int_0^{\varepsilon_f} \frac{f(\sigma_{ij})}{S(T,\dot{\varepsilon})} \mathrm{d}\varepsilon, \qquad \text{(Eq 5)}$$

where ψ_f is the damage value at fracture strain ε_f. Combining Eq 4 and 5, the normalized damage value (D) can be defined as,

$$D = \frac{\psi}{\psi_f} = \int_0^{\varepsilon} \frac{f(\sigma_{ij})}{\psi_f \cdot S(T,\dot{\varepsilon})} \mathrm{d}\varepsilon \qquad \text{(Eq 6)}$$

When the final fracture occurs, the normalized damage value can be evaluated as,

$$\begin{aligned} D|_{\varepsilon=\varepsilon_f} &= \frac{\psi}{\psi_f}|_{\varepsilon=\varepsilon_f} = \int_0^{\varepsilon_f} \frac{f(\sigma_{ij})}{\psi_f \cdot S(T, \ln\ \dot{\varepsilon})} \mathrm{d}\varepsilon \\ &= \frac{1}{\psi_f \cdot S(T, \ln\ \dot{\varepsilon})} \int_0^{\varepsilon_f} f(\sigma_{ij}) \mathrm{d}\varepsilon = 1 \end{aligned} \qquad \text{(Eq 7)}$$

Then Eq 7 can be transferred into,

$$\psi_f \cdot S(T, \ln\ \dot{\varepsilon}) = \int_0^{\varepsilon_f} f(\sigma_{ij}) \mathrm{d}\varepsilon = C \qquad \text{(Eq 8)}$$

As shown in Eq 8, $\psi_f \cdot S(T, \ln \dot{\varepsilon})$ equals to the threshold value C. It is commonly accepted that the Normalized Cockroft-Latham relationships can offer a reasonable prediction

Table 2 Threshold values $C_{N\,C-L}$ under different deformation temperatures and strain rates

Strain rates, s^{-1}	Deformation temperatures, K			
	1123	1223	1323	1373
0.0001	1.96	1.32	1.19	1.0
0.001	0.96	0.77	0.58	0.48
0.01	0.56	0.79	0.63	0.60
0.1	0.67	0.87	0.75	0.57

of the ductile fracture during metal forming. Thus, the Normalized Cockroft-Latham criterion is used to calculate the threshold value C (Ref 6).

$$\int_0^{\varepsilon_f}\left(\frac{\sigma^*}{\bar{\sigma}}\right)d\varepsilon = C_{N\,C-L}, \qquad \text{(Eq 9)}$$

where σ^* is the maximum stress and $\bar{\sigma}$ is the effective stress. $C_{N\,C-L}$ is the threshold value calculated by the Normalized Cockroft-Latham criterion. In cold metal forming, $C_{N\,C-L}$ is usually regarded as a constant. However, this assumption is not applicable in hot metal forming, since the effects of deformation temperature and strain rate on the ductile fracture behaviors cannot be neglected. So, it should be considered in the ductile fracture criterion. Therefore, a function $H(T, \ln\dot{\varepsilon})$ is proposed.

$$H(T, \ln\dot{\varepsilon}) = \psi_f \cdot S(T, \ln\dot{\varepsilon}) = C_{N\,C-L} \qquad \text{(Eq 10)}$$

The function $H(T, \ln\dot{\varepsilon})$ correlates $C_{N\,C-L}$ with deformation temperature and strain rate, and this function can be determined based on the experimental data. Then, the Normalized Cockroft-Latham ductile damage model can be expressed as,

$$D = \frac{\psi}{\psi_f} = \int_0^{\varepsilon}\frac{f(\sigma_{ij})}{\psi_f \cdot S(T, \ln\dot{\varepsilon})}d\varepsilon == \int_0^{\varepsilon}\frac{\sigma^*/\bar{\sigma}}{H(T, \ln\dot{\varepsilon})}d\varepsilon, \qquad \text{(Eq 11)}$$

when D reaches 1, the ductile fracture occurs.

In order to determine the threshold value $C_{N\,C-L}$ under each test condition, finite element simulations for the above hot tensile tests are performed by the commercial software DEFORM-3D. The Normalized Cockroft-Latham criterion is first implemented into DEFORM-3D by the user subroutine. Thus, the values of $\int_0^{\varepsilon}(\sigma^*/\bar{\sigma})d\varepsilon$ can be determined based on the simulated results. The threshold value $C_{N\,C-L}$ is taken as the value of $\int_0^{\varepsilon}(\sigma^*/\bar{\sigma})d\varepsilon$ when the simulated displacement is equal to the experimentally measured fracture displacement. Table 2 shows the obtained values of $C_{N\,C-L}$.

Figure 6 shows the relationship between the threshold value $C_{N\,C-L}$ and deformation conditions. Under relatively high strain rates (0.01 and 0.1 s^{-1}), the value of $C_{N\,C-L}$ first increases, and then decreases with the increase of deformation temperature. However, under relatively low strain rates (0.0001 and 0.001 s^{-1}), the value of $C_{N\,C-L}$ decreases with the increase of deformation temperature. Additionally, there is similar relationship between the fracture strain and deformation conditions. It results from the combined effects of dynamical recrystallization and grain coarsening during the hot deformation.

By the nonlinear fitting method, $H(T, \dot{\varepsilon})$ can be evaluated as,

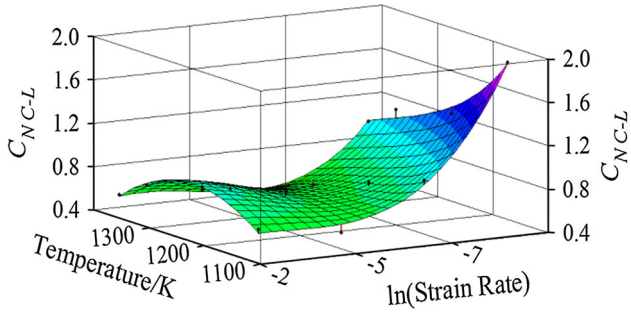

Fig. 6 Relationship between $C_{N\,C-L}$ and deformation conditions

$$\begin{aligned} H(T,\dot{\varepsilon}) = &-108.9 + \frac{3.50\times10^5}{T} - 7.2\times\ln\dot{\varepsilon} - \frac{3.64\times10^8}{T^2} \\ &- 0.19\times(\ln\dot{\varepsilon})^2 + 1.65\times10^4\times\frac{\ln\dot{\varepsilon}}{T} \\ &+ \frac{1.2\times10^{11}}{T^3} - 0.006\times(\ln\dot{\varepsilon})^3 + 144.3\frac{(\ln\dot{\varepsilon})^2}{T} \\ &- 9.6\times10^6\times\frac{\ln\dot{\varepsilon}}{T^2} \end{aligned} \qquad \text{(Eq 12)}$$

Thus, the Normalized Cockroft-Latham ductile damage model for 42CrMo steel can be established as,

$$\begin{cases} D = \int_0^{\varepsilon}\frac{\sigma^*/\bar{\sigma}}{H(T,\ln\dot{\varepsilon})}d\varepsilon \\ H(T,\dot{\varepsilon}) = -108.9 + \frac{3.50\times10^5}{T} - 7.2 \\ \quad\times\ln\dot{\varepsilon} - \frac{3.64\times10^8}{T^2} - 0.19\times(\ln\dot{\varepsilon})^2 + 1.65 \\ \quad\times10^4\times\frac{\ln\dot{\varepsilon}}{T} + \frac{1.2\times10^{11}}{T^3} - 0.006\times(\ln\dot{\varepsilon})^3 \\ \quad + 144.3\frac{(\ln\dot{\varepsilon})^2}{T} - 9.6\times10^6\times\frac{\ln\dot{\varepsilon}}{T^2} \end{cases} \qquad \text{(Eq 13)}$$

4. Verification of the Established Ductile Damage Model

In order to verify the established ductile damage model, Fig. 7 compares the predicted and measured fracture displacements of the hot tensile experiments under deformation temperatures of 1123, 1223, 1323, and 1373 K. Obviously, the predicted fracture displacements well agree with the measured ones. Additionally, the absolute relative errors between the predicted (δ_P) and measured (δ_M) fracture displacements are computed to evaluate the accuracy of the established damage model.

$$\text{Absolute relative error} = \frac{|\delta_P - \delta_M|}{\delta_M}\times 100\,\% \qquad \text{(Eq 14)}$$

Table 3 shows the absolute relative errors between the predicted (δ_P) and measured (δ_M) fracture displacements under the test conditions. It can be found that the averaged

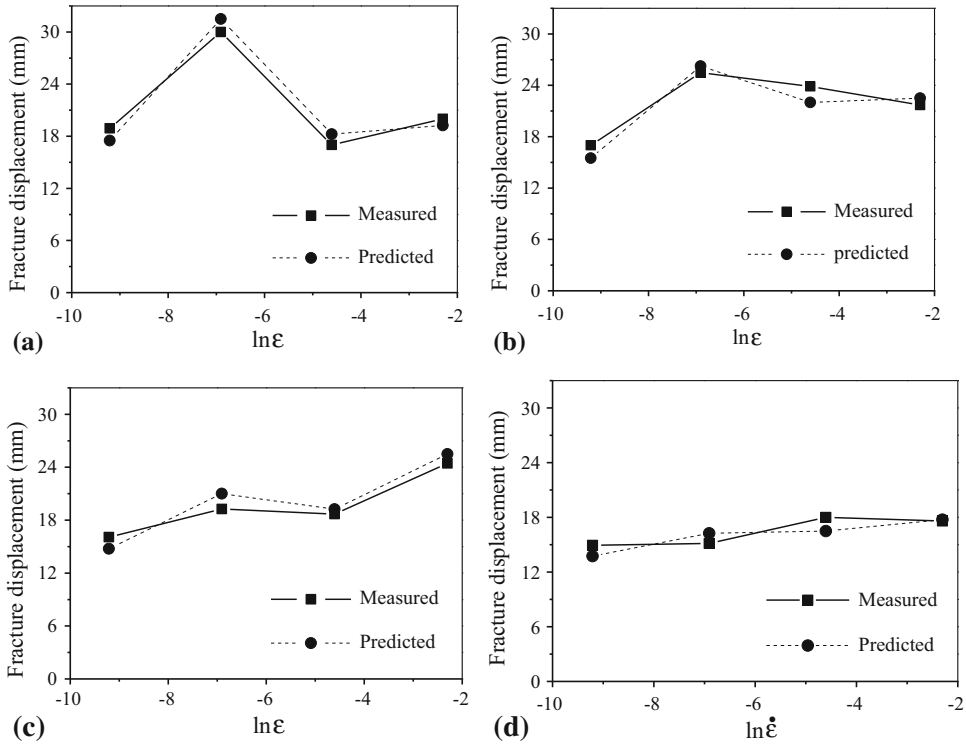

Fig. 7 Comparisons between the predicted and measured fracture displacements under the deformation temperatures of: (a) 1123 K; (b) 1223 K; (c) 1323 K; (d) 1373 K

Table 3 Comparisons between the predicted (δ_P) and measured (δ_M) fracture displacements

Strain rate, s^{-1}	Deformation temperature, K	δ_M, mm	δ_P, mm	Absolute relative error, %
0.0001	1123	18.92	17.50	7.49
	1223	17.00	15.50	8.82
	1323	16.08	14.75	8.27
	1373	14.94	13.75	7.95
0.001	1123	30.00	31.5	5.00
	1223	25.48	26.25	3.02
	1323	21.00	18.50	9.01
	1373	15.14	16.25	7.33
0.01	1123	17.00	18.25	7.35
	1223	23.87	22.00	7.83
	1323	19.25	18.00	3.05
	1373	18.00	16.50	8.33
0.1	1123	20.00	19.25	3.75
	1223	21.70	22.50	3.69
	1323	25.50	23.75	4.34
	1373	17.60	17.75	0.85

absolute relative error is only 6.01%. This result indicates that the established model can give an accurate estimation of the hot tensile fracture behaviors of 42CrMo steel.

5. Application of the Established Ductile Damage Model in Hot Forging Process

In this section, the established ductile damage model is applied in hot forging process. Hot forging experiments and the corresponding finite element simulations are conducted. Figure 8 shows the fracture initiation sites observed in the hot forging experiments and predicted by finite element simulations. Obviously, the observed and predicted results are in a good agreement. The fracture generally occurs in the regions where the workpiece contacts the corners of dies during the hot forging.

In order to further study the damage evolution during the hot forging, the damage degrees at the critical positions (P1, P2, P3, and P4) are tracked, as shown in Fig. 9(a). It can be found that the damage evolutions with the deformation degree at the positions P1, P2, P3, and P4 are similar. Thus, the average damage value of these positions at each simulation step is calculated and can be used to characterize the damage degree of the deformed block. Figure 9(b) shows the variations of the average damage value with deformation degree under the deformation temperatures of 1223 and 1473 K. It can be found that the critical deformation degrees (at which the fracture occurs) under the deformation temperatures of 1223 and 1473 K are 53% and 44%, respectively.

Table 4 shows the comparisons between the predicted and experimental ductile fracture behaviors of 42CrMo steel during the hot forging. In Table 4, 'F' represents the occurrence of ductile fracture, while 'NF' indicates that the ductile fracture does not occur under given deformation conditions. It can be found that, under the deformation temperature of 1223 K, the ductile fracture does not occur when the deformation degree is smaller than 50%, but occurs at 54%. Thus, it can be concluded that the actual critical deformation degree for the ductile fracture falls within the range of 50-54% when the deformation temperature is 1223 K. Similarly, the actual critical deformation degree for the ductile fracture falls within the range of 40-45% when the deformation temperature is 1473 K. These conclu-

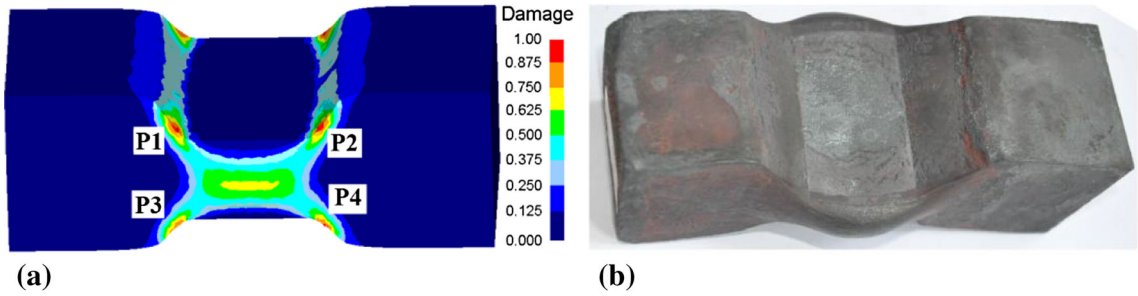

Fig. 8 The facture initiation sites: (a) predicted by finite element simulation; (b) observed in the forging experiment

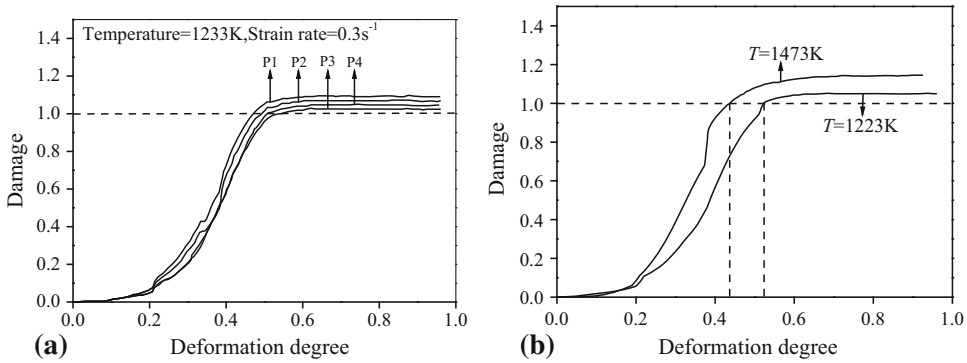

Fig. 9 Damage evolution with deformation degree: (a) at positions P1, P2, P3, and P4; (b) under the deformation temperatures of 1473 and 1223 K

Table 4 Comparisons between the predicted and experimental ductile fracture behaviors

		Ductile fracture	
T, K	Deformation degree, %	Predicted	Experimental
1223	40	NF	NF
	50	NF	NF
	54	F	F
	70	F	F
1473	25	NF	NF
	40	NF	NF
	45	F	F
	54	F	F
	84	F	F

sions are exactly consistent with those from Fig. 9. Also, from Table 4, it can be found that there is a good agreement between the predicted and experimental ductile fracture behaviors. This indicates that the established ductile damage model is capable of predicting the ductile fracture behaviors of 42CrMo steel during hot forging.

6. Conclusions

The hot deformation behaviors of 42CrMo steel are investigated by the tensile tests over wide ranges of deformation temperature and strain rate. Based on the Normalized Cockroft-Latham criterion, a ductile damage model is developed to predict the ductile fracture behaviors of 42CrMo steel during hot deformation. In the developed model, the effects of deformation temperature and strain rate on the critical damage value are considered. The developed model is implemented into the commercial software DEFORM-3D to predict the fracture displacements. There is a good agreement between the predicted and measured fracture displacements. Also, the hot forging experiments and the finite element simulations indicate that the developed ductile damage model is capable of predicting the ductile fracture behaviors of 42CrMo steel in the hot forming process.

Acknowledgments

This work was supported by National Natural Science Foundation of China (Grant No. 51305466, 51375502), National Key Basic Research Program (Grant No. 2013CB035801), and Shenghua Yu-ying Program of Central South University, China.

References

1. Y.C. Lin and X.M. Chen, A Critical Review of Experimental Results and Constitutive Descriptions for Metals and Alloys in Hot Working, *Mater. Des.*, 2011, **32**, p 1733–1759
2. Y.C. Lin, J. Deng, Y.Q. Jiang, D.X. Wen, and G. Liu, Hot Tensile Deformation and Fracture Characteristics of a Typical Ni-based Superalloy at Elevated Temperature, *Mater. Des.*, 2014, **55**, p 949–957
3. Y.C. Lin, J. Deng, Y.Q. Jiang, D.X. Wen, and G. Liu, Effects of Initial δ Phase on Hot Tensile Deformation Behaviors and Fracture Character-

istics of a Typical Ni-based Superalloy, *Mater. Sci. Eng. A*, 2014, **598**, p 251–262
4. J. Lemaitre, *A Course on Damage Mechanics*, Springer, Berlin, 1992
5. A.M. Freudenthal, *The Inelastic Behavior of Solids*, Wiley, New York, 1950
6. M.G. Cockcroft and D.J. Latham, Ductility and the Workability of Metals, *J. Inst. Met.*, 1968, **96**, p 33–39
7. Y.F. Xia, G.C. Luo, D.S. Wu, G.Z. Quan, and J. Zhou, The Evaluation of Varying Ductile Fracture Criteria for $3Cr_{20}Ni_{10}W_2$ Austenitic Heat-Resistant Alloy, *Adv. Mech. Eng.*, 2013, doi:10.1155/2013/520127
8. S. Alexandrov, Y. Mustafa, and M.Y. Yahya, An Efficient Approach for Identifying Constitutive Parameters of the Modified Oyane Ductile Fracture Criterion at High Temperature, *Math. Probl. Eng.*, 2013, doi: 10.1155/2013/514945
9. X.M. Zhang, W.D. Zeng, Y. Shu, Y.G. Zhou, Y.Q. Zhao, H. Wu, and H.Q. Yu, Fracture Criterion for Predicting Surface Cracking of Ti40 Alloy in Hot Forming Processes, *Trans. Nonferr. Met. Soc. China*, 2009, **19**, p 267–271
10. J. He, Z.S. Cui, F. Chen, Y.H. Xiao, and L.Q. Ruan, The New Ductile Fracture Criterion for $30Cr_2Ni_4MoV$ Ultra-Super-Critical Rotor Steel at Elevated Temperatures, *Mater. Des.*, 2013, **52**, p 547–555
11. W.J. Kim, H.K. Kim, W.Y. Kim, and S.W. Han, Temperature and Strain Rate Effect Incorporated Failure Criteria for Sheet Forming of Magnesium Alloys, *Mater. Sci. Eng. A*, 2008, **488**, p 468–474
12. J. Yoon and Y. Lee, Fracture Mechanism of Mg-3Al-1Zn Sheet at the Biaxial State with Respect to Forming Temperatures, *Mater. Des.*, 2014, **55**, p 43–49
13. S.K. Paul, Micromechanics Based Modeling of Dual Phase Steels: Prediction of Ductility and Failure Modes, *Comput. Mater. Sci.*, 2012, **56**, p 34–42
14. S.K. Paul and A. Kumar, Micromechanics Based Modeling to Predict Flow Behavior and Plastic Strain Localization of Dual Phase Steels, *Comput. Mater. Sci.*, 2012, **63**, p 66–74
15. F.M. Shore, M. Morakabati, S.M. Abbasi, and A. Momeni, Hot Deformation Behavior of Incoloy 901 Through Hot Tensile Testing, *J. Mater. Eng. Perform.*, 2014, **23**, p 1424–1433
16. H. Zoghi, A.F. Arezoodar, and M. Sayeaftabi, Enhanced Finite Element Analysis of Material Deformation and Strain Distribution in Spinning of 42CrMo Steel Tubes at Elevated Temperature, *Mater. Des.*, 2013, **47**, p 234–242
17. Y.C. Lin, M.S. Chen, and J. Zhong, Effects of Deformation Temperatures on Stress/Strain Distribution and Microstructural Evolution of Deformed 42CrMo Steel, *Mater. Des.*, 2009, **30**, p 908–913
18. Y.C. Lin and G. Liu, Effects of Strain on the Workability of a High Strength Low Alloy Steel in Hot Compression, *Mater. Sci. Eng. A*, 2009, **523**, p 139–144
19. Y.C. Lin and M.S. Chen, Numerical Simulation and Experimental Verification of Microstructure Evolution in a Three-Dimensional Hot Upsetting Process, *J. Mater. Process. Technol.*, 2009, **209**, p 4578–4583
20. Y.C. Lin, M.S. Chen, and J. Zhong, Study of Static Recrystallization Kinetics in a Low Alloy Steel, *Comput. Mater. Sci.*, 2008, **44**, p 316–321
21. Y.C. Lin and M.S. Chen, Study of Microstructural Evolution During Static Recrystallization in a Low Alloy Steel, *J. Mater. Sci.*, 2009, **44**, p 835–842
22. G.Z. Quan, Y. Wang, Y.Y. Liu, and J. Zhou, Effect of Temperatures and Strain Rates on the Average Size of Grains Refined by Dynamic Recrystallization for As-Extruded 42CrMo Steel, *Mater. Res.*, 2013, **16**, p 1092–1105
23. M.S. Chen, Y.C. Lin, and X.S. Ma, The Kinetics of Dynamic Recrystallization of 42CrMo Steel, *Mater. Sci. Eng. A*, 2012, **556**, p 260–266
24. Y.C. Lin, M.S. Chen, and J. Zhong, Microstructural Evolution in 42CrMo Steel During Compression at Elevated Temperatures, *Mater. Lett.*, 2008, **62**, p 2132–2135
25. Y.C. Lin, M.S. Chen, and J. Zhong, Study of Metadynamic Recrystallization Behaviors in a Low Alloy Steel, *J. Mater. Process. Technol.*, 2009, **209**, p 2477–2482
26. Y.C. Lin and M.S. Chen, Study of Microstructural Evolution During Metadynamic Recrystallization in a Low Alloy Steel, *Mater. Sci. Eng. A*, 2009, **501**, p 229–234
27. H.P. Qi and Y.T. Li, Metadynamic Recrystallization of the As-Cast 42CrMo Steel after Normalizing and Tempering During Hot Compression, *Chin. J. Mech. Eng.*, 2012, **25**, p 853–859
28. Y.C. Lin, X.M. Chen, D.X. Wen, and M.S. Chen, A Physically-Based Constitutive Model for a Typical Nickel-Based Superalloy, *Comput. Mater. Sci.*, 2014, **83**, p 282–289
29. Y.C. Lin, M.S. Chen, and J. Zhong, Constitutive Modeling for Elevated Temperature Flow Behavior of 42CrMo Steel, *Comput. Mater. Sci.*, 2008, **42**, p 470–477
30. Y.C. Lin, M.S. Chen, and J. Zhong, Prediction of 42CrMo Steel Flow Stress at High Temperature and Strain Rate, *Mech. Res. Comm.*, 2008, **35**, p 142–150
31. Y.Y. Li, S.D. Zhao, S.Q. Fan, and B. Zhong, Plastic Properties and Constitutive Equations of 42CrMo Steel During Warm Forming Process, *Mater. Sci. Technol.*, 2014, **30**, p 645–652
32. J.D. Chen, W.L. Mo, P. Wang, and S.P. Lu, Effects of Tempering Temperature on the Impact Toughness of Steel 42CrMo, *Acta Metall. Sin.*, 2012, **48**, p 1186–1193
33. Y.Y. Li, S.D. Zhao, S.Q. Fan, and G.H. Yan, Study on the Material Characteristic and Process Parameters of the Open-Die Warm Extrusion Process of Spline Shaft with 42CrMo Steel, *J. Alloys Compd.*, 2013, **571**, p 12–20
34. L. Wang, D.S. Qian, J. Guo, and Y. Pan, Austenite Grain Growth Behavior of AISI, 4140 Alloy Steel, *Adv. Mech. Eng.*, 2013, doi: 10.1155/2013/762890
35. G. Zhou, L. Hua, and D.S. Qian, 3D Coupled Thermo-Mechanical FE Analysis of Roll Size Effects on the Radial-Axial Ring Rolling Process, *Comput. Mater. Sci.*, 2011, **50**, p 911–924
36. G.Z. Quan, G.C. Luo, A. Mao, J.T. Liang, and D.S. Wu, Evaluation of Varying Ductile Fracture Criteria (VDFC) for 42CrMo Steel by Compressions at Different Temperatures and Strain Rates, *World J. Sci.*, 2014, doi:10.1155/2014/579328
37. ISO 6892-2: Metallic Materials—Tensile Testing—Part 2: Method of Test at Elevated Temperature, 2011
38. H. Mirzadeh, Constitutive Analysis of Mg-Al-Zn Magnesium Alloys During Hot Deformation, *Mech. Mater.*, 2014, **77**, p 80–85
39. I. Balasundar, T. Raghu, and B.P. Kashyap, An Unified Constitutive Equation to Predict the High Temperature Flow Stress of Near Alpha Titanium Alloy Titan 29A in +Regime, *Int. J. Adv. Eng. Appl.*, 2013, **2**, p 21–27
40. V. Torabinejad, A. Zarei-Hanzaki, and S. Moemeni, An Analysis to the Kinetics of Austenite Recrystallization in Fe-30Mn-5Al Steel, *Mater. Manuf. Process.*, 2012, **28**, p 36–41
41. D.Z. Li, Y.H. Wei, C.Y. Liu, and L.F. Hou, Hot Deformation Behaviors of Fe-30Mn-3Si-3Al TWIP Steel During Compression at Elevated Temperature and Strain Rate, *Steel Res. Int.*, 2013, **84**, p 740–750
42. H. Guler, R. Ertan, and R. Ozcan, Investigation of the Hot Ductility of a High-Strength Boron Steel, *Mater. Sci. Eng. A*, 2014, **608**, p 90–94
43. Z.H. Wang, S.H. Sun, B. Wang, Z.P. Shi, R.H. Zhang, and W.T. Fu, Effect of Grain Size on Dynamic Recrystallization and Hot-Ductility Behaviors in High-Nitrogen CrMn Austenitic Stainless Steel, *Metall. Mater. Trans. A*, 2014, **45**, p 3631–3639
44. I. Balasundar, T. Raghu, and B.P. Kashyap, Modeling the Hot Working Behavior of Near-α Titanium Alloy IMI834, *Prog. Nat. Sci.: Mater. Int.*, 2013, **23**, p 598–607
45. F.M. Shore, M. Morakabati, S.M. Abbasi, A. Momeni, and R. Mahdavi, Hot Ductility of Incoloy 901 Produced by Vacuum Arc Remelting, *ISIJ Int.*, 2014, **54**, p 1353–1360
46. A.E. Salas-Reyes, I. Mejía, A. Bedolla-Jacuinde, A. Boulaajaj, J. Calvo, and J.M. Cabrera, Hot Ductility Behavior of High-Mn Austenitic Fe-22Mn-1.5Al-1.5Si-0.45C TWIP Steels Microalloyed with Ti and V, *Mater. Sci. Eng. A*, 2014, **611**, p 77–89
47. F.M.A. Pires, J.M.A.C. de Sá, L.C. Sousa, and R.M.N. Jorge, Numerical Modelling of Ductile Plastic Damage in Bulk Metal Forming, *Int. J. Mech. Sci.*, 2003, **45**, p 273–294
48. U.F. Kocks, Laws for Work Hardening and Low Temperature Creep, *J. Eng. Mater. Technol.*, 1976, **98**, p 76–85